Possible Explosive Dispersal Outflow in IRAS 16076-5134 revealed with ALMA

Estrella Guzmán Ccolque,[1] Manuel Fernández-López,[2] Luis A. Zapata,[3] and Tapas Baug[4]

[1]*Instituto Argentino de Radioastronomía (CCT- La Plata, CONICET,CICPBA)*
C.C. No. 5,1894, Villa Elisa, Buenos Aires, Argentina
[2]*Instituto Argentino de Radioastronomía (CCT- La Plata, CONICET,CICPBA), C.C. No. 5,1894, Villa Elisa, Buenos Aires, Argentina*
[3]*Instituto de Radioastronomía y Astrofísica. Universidad Nacional Autónoma de México, P.O. Box 3-72,58090, Morelia,*
Michoacán,México
[4]*S. N. Bose National Centre for Basic Sciences, Block-JD, Sector-III, Salt Lake, Kolkata 700106, India*

ABSTRACT

We present 0.9 mm continuum and CO (3-2) line emission observations retrieved from the Atacama Large Millimeter/submillimeter Array (ALMA) archive toward the high-mass star formation region IRAS 16076-5134. We identify fourteen dense cores with masses between 0.3 to 22 $M_\odot$. We find an ensemble of filament-like CO (3-2) ejections from -62 to $+83$ km s^{-1} that appear to arise radially from a common central position, close to the dense core MM8. The ensemble of filaments, has a quasi-isotropic distribution in the plane of the sky. The radial velocity of several filaments follow a linear velocity gradient, incresing from a common origin. Considering the whole ensemble of filaments, we estimate its total mass to be 138 and 216 $M_\odot$ from its CO emission, for 70 K and 140 K respectively. Also, assuming a constant velocity expansion of the filaments (of 83 km s^{-1}) we estimate the dynamical age of the outflowing material (3500 years), its momentum ($\sim 10^4$ $M_\odot$ km s^{-1}) and its kinetic energy ($\sim 10^{48-49}$ erg). The morphology and kinematics presented by the filaments suggest the presence of a dispersal outflow with explosive characteristics in IRAS 16076-5134. In addition, we make a raw estimate of the lower limit of the frequency rate of the explosive dispersal outflows in the Galaxy (one every 110 years) considering constant star formation rate and efficiency with respect to the galactocentric radius of the Galaxy. This may imply a comparable rate of dispersal outflows and supernovae (approximately one every 50 years), which may be important for the energy budget of the Interstellar Medium and the link between dispersal outflows and high-mass star formation.

Keywords: Star formation, Interstellar dynamics, Interferometers, Submillimeter Astronomy

1. INTRODUCTION

IRAS 16076-5134 or AGAL 331.28-00.19 (hereafter I16076) is an ultracompact HII (UCHII) region located at 5.0±0.7 kpc (Baug et al. 2020, kinematic distance calculated using the Kinematic Distance Calculation Tool of Wenger et al. (2018)). This measure is similar to the value obtained previously by Faúndez et al. (2004) (5.2 kpc), derived using a flat rotation model of the Milky Way and the CS(2-1) line velocity reported by (Bronfman et al. 1996). I16076 has FIR color typical of UCHII regions (Wood & Churchwell 1989). Faúndez et al. (2004) detected its dust emission at 1.2 mm, measuring its size (38″), dust temperature (33 K) and mm-

estreguzman@gmail.com

IR bolometric luminosity (2.0×10^5 $L_\odot$). Such large mm-IR bolometric luminosity in a cold dust region usually implies its link with a region forming one or more stars of spectral types B and O. A dense clump (radius=1.57 pc) in I16076 was also observed in the ATLASGAL survey at 870 μm for which Urquhart et al. (2018) presented values of H_2 column density (23.3×10^{15} cm^{-2}), mass (45.6 $M_\odot$) and dust temperature (30.1 K). In addition, they used a combination of archival observations from molecular line surveys reported in the literature (such as CO, NH$_3$, CS, etc) to determine the radial velocity with regard to the local standard of rest (v_{lsr}): -87.7 km s^{-1}. I16076 shows strong blueshifted emission profile of HCN(4-3), known to be a tracer of infalling gas and therefore an indicator of accretion processes (Liu et al. 2016). More recently, I16076 was observed with ALMA at 3 mm in

order to explore the molecular outflows in this region Liu et al. (2020). Baug et al. (2020) detected several outflow lobes in CO (3-2) toward IRAS16076. Most of them are associated with the millimeter sources identified by Baug et al. (2021). In particular, from the dense core identified as I16076_O1 seem to arise 19 outflow lobes (9 redshifted and 10 blueshifted) distributed almost isotropically. This morphology is reminiscent of the dispersal outflows with explosive features detected in Orion BN/KL, DR21 and G5.89-0.39 (Bally et al. 2015, 2017; Zapata et al. 2017, 2019, 2020). Hereafter we refer to this type of outflows as 'explosive dispersal outflows'or just 'dispersal outflows'.

Since their discovery, explosive dispersal outflows have become a new subclass of molecular outflows observed in the star-forming regions of massive stars (e.g., Zapata et al. 2009). At present, there seem to be two types of molecular outflows. The first type is the classical outflows which are typically bipolar, produced mostly by low-mass stars in their formation process (Arce et al. 2007). Theoretical work suggests that this outflows are intimately related to the accretion process and play an important role in dissipating excess angular momentum in the infalling material and allow the star to build up its mass through accretion (e.g., Shu et al. 1987, 1991, 2000; Konigl & Pudritz 2000). On the other side, the dispersal outflows with explosive characteristics, whose nature is still unknown (Bally & Zinnecker 2005; Zapata et al. 2009; Bally et al. 2011, 2017). They have been associated to an energy release produced by the disintegration or close encounters of young stellar systems (Bally et al. 2017; Rivera-Ortiz et al. 2021) or the merger of several massive protostars (Bally & Zinnecker 2005). These outflows appear to be impulsive and created by a single brief energetic event with energy injections of about 10^{47-49} erg (Bally & Zinnecker 2005). They comprise dozens of filament-shaped ejections isotropically distributed on the sky. Each filament follows a well-defined Hubble velocity law, that is the radial velocities linearly increase with projected distances (Zapata et al. 2009, 2013; Bally et al. 2017; Zapata et al. 2019). Dispersal outflows are usually detected by their CO emission (Peng et al. 2012; Zapata et al. 2017, 2019, 2020) but they have also been detected in H_2 (Bally et al. 2011), and [FeII] condensations have been observed at the tips of the filaments in the case of Orion BN/KL (Bally et al. 2015).

Zapata et al. (2017) enumerated four clear morphological and kinematical features of explosive dispersal outflows that distinguishes them from classical bipolar molecular outflows:

- The explosive dispersal outflows consist of narrow straight filament-like ejections with different orientations and an almost isotropic distribution.

- The filaments point back to common position where the explosive event may have occurred.

- The radial velocity of each filament increases linearly with distance projected on the sky from the origin, it seems to follow a Hubble's law.

- The redshifted and blueshifted filaments seem to overlap in the plane of the sky.

Moreover:

- These outflows are associated with regions of high-mass star formation.

- Their energies are in the range of $10^{47} - 10^{49}$ erg.

Using observations from the ALMA archive, and following the features of explosive dispersal outflows described in (Zapata et al. 2017) we propose the possible presence of this type of event in I16076. We reanalyze the dust and line kinematics of the ALMA data under this hypothesis, and present the new implications of the discovery. The paper is organized as follows. In Section 2 we present the ALMA observations. The identification and derivation of the physical parameters of the 0.9 mm continuum sources, as well as of the CO (3-2) filamentary ejections are presented in Section 3. A brief discussion on whether I16076 is an explosive dispersal outflow, and the rate of such events in the Galaxy can be found in Section 4. The conclusions of this study are presented in Section 5.

2. ALMA OBSERVATIONS

The Band 7 observations were carried out during ALMA (Atacama Large Millimeter/submillimeter Array) Cycle 5, as part of the program 2017.1.00545.S (P.I: Tie, Liu). The array was in C43-2 configuration, with 48 12-m antennas available at the time, and a baseline ranging 15-314 m. The I16076 data presented in this article correspond to a portion of a larger program, comprising 10 more sources. I16076 was observed in three sessions (Table 1) during May 2018, totaling approximately 21 minutes on source under good weather conditions, with precipitable water vapor (PWV) around 0.4 mm. The observations were made in mosaic mode with 17 pointings covered during each individual session. The coordinates of the mosaic center were $(\alpha, \delta)_{J2000.0} = 16^h11^m27.1^s, -51°41'55.1''$.

The correlator was configured to use four spectral windows centered at 343.302, 345.183, 354.505 and

356.840 GHz. The former two were used to image the continuum and ^{12}CO(3-2) emission, respectively; they had a 0.976 MHz spectral resolution and a total bandwidth of 1.875 GHz. The remaining spectral windows aimed at the HCN(4-3) and HCO(4-3) lines; they had a 0.244 MHz (0.85 km s^{-1} at the observing frequency) spectral resolution and a total bandwidth of 0.469 GHz. In this work, we focus on the 0.9 mm continuum and the CO (3-2) line emission. J1650-5044 was used as the phase calibrator, J1427-4206 and J1517-2422 as the bandpass and flux calibrator. The estimation for the absolute flux calibration these frequency in ALMA is $\sim 10\%$[1].

Visibility data were reduced using CASA 5.1.1 (Common Astronomy Software Applications) package. First, the data were calibrated by running the calibration script provided by the ALMA staff. The images were constructed using *tclean* task of the CASA version 6.1.2. The cleaning process was performed interactively applying the Hogbom minor cycle algorithm and Briggs weighting, setting the robust parameter to 0.5, which ensures a good compromise between the sensitivity and the angular resolution of the images. The rms of the continuum image is 1.3 mJy beam^{-1} and the angular resolution is $0\rlap.{''}8 \times 0\rlap.{''}7$ (PA= 74°.6; where PA is the position angle [2]). For the CO cube the rms is 5.6 mJy beam^{-1} per channel and the angular resolution is $0\rlap.{''}9 \times 0\rlap.{''}8$ (PA=80°.6).

3. RESULTS

3.1. *Submillimeter Continuum Sources*

Figure 1 shows the positions of fourteen 0.9 mm continuum sources detected with ALMA in I16076. These sources are labeled as MM sources sorted by their Right Ascension. We consider a flux density threshold of $5\sigma \sim 7$ mJy beam^{-1} as a criterion to visually identify continuum peaks, which we associate with continuum sources (here σ is estimated analyzing the empty background emission). The continuum map shows the sources are mainly distributed in two small clusters. One small cluster around MM3, and a larger one around MM8. Table 2 presents some parameters to characterize these continuum sources, including central coordinates, deconvolved sizes, peak intensities, flux densities and masses. These parameters, except for the mass, and

their uncertainties were estimated fitting 2D-Gaussians by using the CASA task imfit. Since the sizes of the millimeter sources are of the order of ~ 0.1 pc, we assume that they correspond to dense cores[3]. MM1, MM3, MM5, MM7, MM8 and MM9 were previously identified by Baug et al. (2021), who also considered these sources as dense cores.

We calculate the masses of the dense cores using:

$$M_{core} = \frac{F_\nu d^2 R}{B_\nu(T_d)\,\kappa_\nu} \qquad (1)$$

where F_ν is the observed total flux density, B_ν is the Planck function for a dust temperature T_d, d is the distance to the source, R is the dust-to-gas mass ratio and k_ν is the dust opacity which depends on the frequency as $\kappa_\nu = \kappa_o \cdot (\nu/\nu_o)^\beta$. We assume that the dust emission is isothermal and optically thin and neglect any possible effects produced by scattering. Therefore, all the masses presented should be considered as lower limits. We adopt the same assumptions as in Fernández-López et al. (2021), who studied the massive star-forming region G 5.89-0.39, also associated with an explosive dispersal outflow. Hence, assuming that I16076 is a region similar to G5.89, we consider $\beta=$ 2.0, a dust with thin ice mantles with 10^6 cm^{-3} density, and a gas-to-dust ratio of 100. Interpolating the dust opacity models of Ossenkopf & Henning (1994) to the observed wavelenght we obtain an opacity of 1.80 cm^2 g^{-1} at 0.9 mm. Since we do not have a measurement of the dust temperature in the dense cores of I16076 we fix their mean dust temperature to $T_d = 30$ K (measured temperature for the dense clump of IRAS16076 reported by Urquhart et al. (2018)). The estimated masses of the dense cores range from 0.3 to 22 $M_\odot$ (see Table 2). To obtain the uncertainty in the masses we only considered errors in the total observed flux density. MM7, MM8 and MM9 cores are among the most massive, with masses greater than 10 $M_\odot$. The masses we obtained are lower by a factor of 3 than the masses of the dense cores estimated by Baug et al. (2021). The reason for the discrepancies resides in the opacity, that they estimated using an expression of Hildebrand (1983), which resulted a factor of 3 higher than ours. In addition, they warned that their larger masses had to be taken with caution, as the low

---

[1] See Section 10.4.7 in the ALMA Cycle 8 Technical Handbook

[2] PA is the measured angle of the beam's major axis with respect to the north celestial pole, turning positive in the right ascension direction (i.e., toward East).

[3] We use the nomenclature and definition in Zhang et al. (2009), Motte et al. (2018), Bally et al. (2017) and Hull et al. (2014), who refer as clouds to 10-100 pc structures, molecular clumps to 1 pc structures where populations of both massive and lower mass stars are formed, dense cores to 0.01-0.1 pc structures forming one or a group of stars; and protostellar envelopes to 1000 AU (~ 0.005 pc) structures comprising the densest parts of the dense core, inside which one or several protostars are formed.

Table 1. Summary of Band 7 ALMA Observations of IRAS16076-5134 (Project 2017.1.00545.S)

Execution Blocks IDs	uid://A002/Xcda49e/Xb713	uid://A002/Xcda49e/Xc0a3	uid://A002/Xcdb7b8/Xd8c8
Observation date	2018-05-21	2018-05-21	2018-05-23
Number of antennas	48	48	45
Time on Source (sec)	428.2	428.3	428.2
Mean PWV(mm)	0.4	0.5	0.3
Phase Calibrator	J1650-5044	J1650-5044	J1650-5044
Bandpass Calibrator	J1427-4206	J1427-4206	J1517-2422
Flux Calibrator	J1427-4206	J1427-4206	J1517-2422
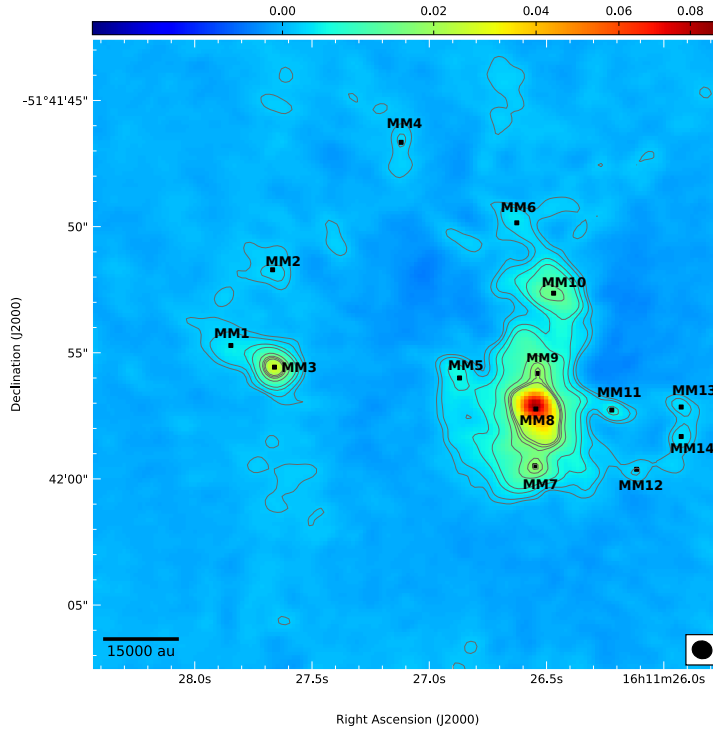
Figure 1. 0.9 mm continuum emission toward IRAS 16076-5143 in colour-scale and grey contours (at 3,5,10,15,30,40,45 times the rms noise level of 4 mJy beam^{-1}). The synthesized beam, in the bottom right corner, is $0\rlap{.}''8 \times 0\rlap{.}''7$, PA= $74^\circ.6$. The submillimeter continuum sources identified here are marked by black dots.

angular resolution could hinder multiple systems to be marginally resolved. Such as the case of I16076-O1 in which we detect three possible dense cores (MM7, MM8 and MM9) or as I16076-O3 composed of MM1 and MM3.

3.2. Outflow Identification and Kinematics

In Figure 2 we present the CO (3-2) molecular emission in the range of radial velocities from -62.15 to 83.47 km s^{-1}, avoiding the central velocity channels ([-5.5:6.2] km s^{-1}) that show extended CO emission from the cloud (velocities expressed with respect to

Table 2. Submillimeter Continuum Sources in I16076

Source	RA	DEC	Deconvolved Size	Peak Intensity	Flux Density	Mass	Name Baug
	[ICRS]	[ICRS]	[$'' \times ''$, $°$]	[mJy beam^{-1}]	[mJy]	[M$_\odot$]	
MM1	16:11:27.758±0.008	-51:41:55.01±0.03	3.8±0.2×1.10±0.06, 77±1	4.0±0.2	38±2	2.9±0.1	I16076_O3
MM2	16:11:27.668±0.008	-51:41:51.71±0.07	1.4±0.2×1.1±0.2, 50±70	2.5±0.3	9±1	0.7±0.1	––
MM3	16:11:27.660±0.001	-51:41:55.57±0.01	0.87±0.01×0.70±0.05, 50±20	26.5±0.7	56±2	4.3±0.2	I16076_O3
MM4	16:11:27.120±0.002	-51:41:46.66±0.05	1.5±0.1×0.5±0.2, 176±3	2.2±0.1	5.7±0.5	0.44±0.04	––
MM5	16:11:26.870±0.007	-51:41:55.99±0.07	1.5±0.2×0.9±0.2, 40±20	5.2±0.6	18±2	1.4±0.2	I16076_O4
MM6	16:11:26.626±0.009	-51:41:49.85±0.08	1.7±0.3×0.9±0.2, 50±10	3.2±0.4	12±2	0.9±0.1	––
MM7	16:11:26.550±0.001	-51:41:59.48±0.01	1.36±0.03×1.11±0.03, 162±6	18.2±0.3	69±2	5.3±0.1	I16076_O1
MM8	16:11:26.546±0.005	-51:41:57.23±0.06	1.6±0.2×1.1±0.1, 20±10	70.4±6.0	290±30	22±1	I16076_O1
MM9	16:11:26.5392±0.0003	-51:41:55.820±0.006	2.27±0.01×0.981±0.008, 178.1±0.3	18.5±0.1	101.1±0.7	5.7±0.3	I16076_O1
MM10	16:11:26.474±0.004	-51:41:52.64±0.03	2.1±0.1×1.11±0.06, 58±3	13.9±0.6	74±3	5.7±0.3	––
MM11	16:11:26.222±0.008	-51:41:57.27±0.03	point source	5.6±0.4	7±1	0.54±0.08	––
MM12	16:11:26.12±0.01	-51:41:59.62±0.04	1.1±0.3×0.4±0.2, 100±10	2.2±0.3	4±1	0.31±0.06	––
MM13	16:11:25.929±0.003	-51:41:57.12±0.02	1.2±0.1×0.4±0.1, 50±10	5.7±0.6	2.7±0.2	0.44±0.01	––
MM14	16:11:25.926±0.003	-51:41:58.32±0.04	1.1±0.1×0.45±0.1, 160±10	2.9±0.2	6±1	0.46±0.05	––

NOTE—Masses estimated using dust temperatures of 30 K. The last column shows the labels of the dense cores identified by Baug et al. (2021).

the cloud velocity, $v_{sys}=-87.70$ km s^{-1}[4]). We perform the identification of the outflow filaments using Miriad's `cgcurs`[5] task (Sault et al. 1995). We manually obtained the positions and line-of-sight velocities of all half-beam (0.5 arcsec) condensations where the CO emission, in all pixels belonging to the condensation, is greater than 3σ (34 mJy beam^{-1}). Each condensation is marked with a red/blue dot in case its velocity is redshifted/blueshifted. This procedure was repeated for each channel of the CO data cube, except for the central channels where the cloud emission was predominant and the channels with absorption features at 23.4 and 44.5 km s^{-1} (see Fig. 3). These absorption features may be due to colder and overlapping foreground molecular clouds along the line of sight, and are out of the scope of this contribution. In addition, the ALMA spectrum reveals other weak emission lines from other chemical species (CH$_3$OH, ^{34}SO$_2$, HC$_3$N, CH$_3$CHO), which are not focus of the present work. After collecting the positions for the CO (3-2) condensations we continued to building up a map in which dozens of filament-like structures can be distinguished emerging quasi-radially from a common center near the MM8 peak. Two more north-

south extended monopolar filaments (one blueshifted to the south and one redshifted to the north) can be seen East of the filaments associated to MM8. The blueshifted filament, with a length of $\sim 11''$, seems to be associated with the MM3 core. The association of the northern redshifted filament ($\sim 18''$ in length) with a dense core is not clear, although Baug et al. (2020) attributed it to the I16076-O2 core. In this work, we focus on the analysis of the 24 radial filaments identified around MM8. We found 12 blueshifted and 12 redshifted filaments (see Figure 4). Most of them coincide with outflows reported by Baug et al. (2020), and associated with the dense core IRAS16076-O1 (resolved into MM7, MM8, MM9 in our work). Filament parameters, such as terminal velocity, coordinates of its outer tip, length and position angle (PA) are given in Table 3. Some of the filaments show very high radial velocities (v>50 km s^{-1}), while others are more quiescent (v<10 km s^{-1}). They show a wide range of PA values, indicating that, if they are somehow related, they do not have a preferred direction.

Figure 5 shows a diagram with the line-of-sight velocity as function of the projected distance (PV diagram) of the CO molecular condensations traced by the filaments around MM8 (up to a projected distance <15''). The redshifted and blueshifted filaments are distinguished by red and blue dots, respectively. As said before, no molecular condensations were marked around 0 km s^{-1} due to extended emission contamination. In addition, extended emission is also observed at 42.4 km s^{-1} throughout the field of view. These can be explained by the presence of

[4] Throughout this paper, we work with radial (or line-of-sight) velocities, v, with respect to the cloud velocity, unless otherwise noted.

[5] Cgcurs displays an image displays an image and allows to interactively read image values, evaluate statistics within a poligonal region that can be interactively defined and recorded into a text file.
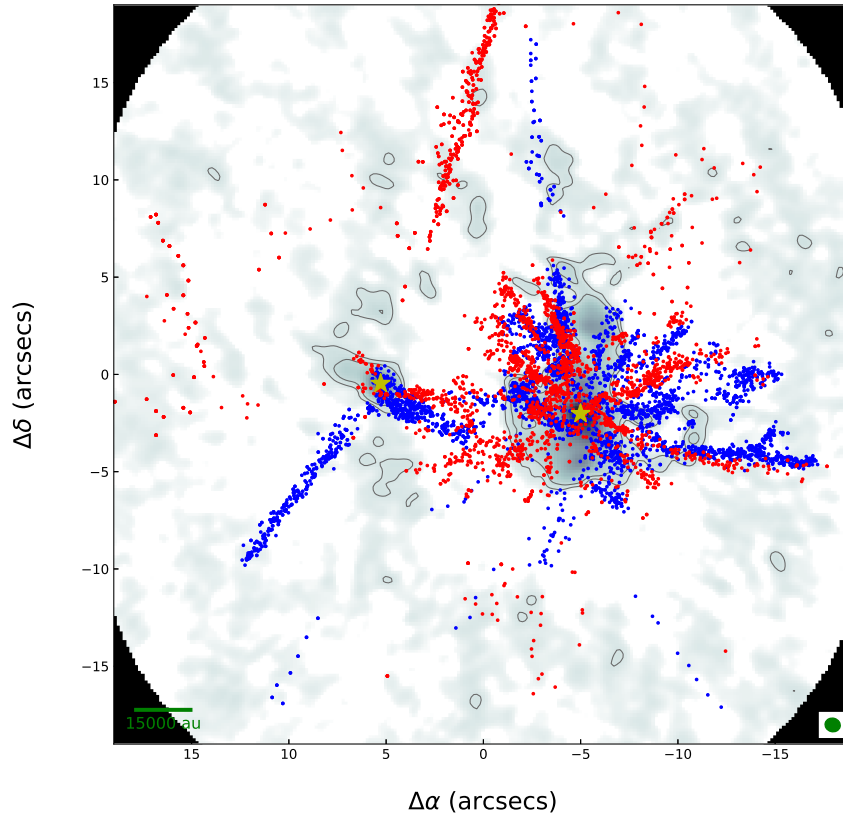
Figure 2. Image of the molecular outflows in IRAS 16076-5134. Background grey-scale image is the ALMA 0.9 mm continuum image from Figure 1 and the black contours are set at 3 and 6 times the rms noise level. The red and blue circles correspond to redshifted and blueshifted CO(3-2) gas condensation, identified in the velocity cubes as part of the outflows in the region (see Section 3.2). The driving sources of the ensemble of filaments (West) and the blueshifted monopolar outflow lobe (East) are marked with yellow stars.

other emitting cloud along the line-of-sight, whose extended emission is filtered by the interferometer, hindering the spatial distribution of the filament's from I16076. The emission from filaments with gas at higher velocities appears more compact (filaments with projected lengths $<2''$) and close to the origin of the filaments, near the position of MM8. The black and green arrows join the central position (the peak of the MM8 core at 0 km s^{-1}) and the tip of each filament (see Table 3). The current angular resolution of the observations does not allow the kinematics of the filaments to be adequately analyzed from the PV diagram.

A 3D representation of the 24 CO (3-2) filaments ensemble toward I16076 gives a better idea of the isotropic morphology and its ordered kinematic pattern (Figure 6). The X and Y axis in this graphic are the projected distance in RA and DEC (in $''$), while the Z axis represents the radial velocity (in km s^{-1}) of the filaments,

which is also displayed by a color scale. The central position is at $(\alpha, \delta)_{J2000.0} = 16^h 11^m 26.546^s, -51°41'57.23''$ (the MM8 core position). For this image to represent the actual 3D distribution of the filaments, the filaments should be undergoing an expansive motion at constant velocity following ballistic trajectories. Assuming this, the Figure 6 would provide a general view of the spatial distribution and kinematics of the filaments ensemble. As can be seen in Figure 2, 4 and 6, one of the main characteristics of the filaments is their quasi-isotropic distribution on the plane of the sky projected. They also appear to have a common origin in space and velocity. Furthermore, the velocity within most of the filaments become bluer or redder with the distance from the origin. This indicates that the filaments presents a velocity gradient. Although a velocity gradient similar to a Hubble's law is observed, this does not imply that filaments are currently undergoing acceleration. Since no clear ac-
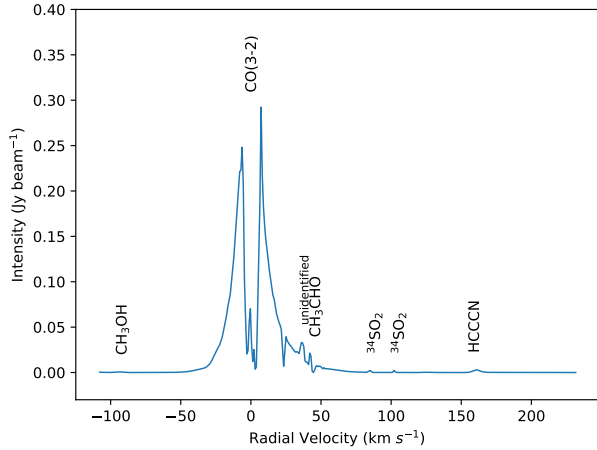
Figure 3. CO (3-2) spectrum integrated over the whole ensemble of filaments associated with MM8. The radial velocity is expressed relative to the system cloud velocity of -87.7 km s^{-1}. The spectrum shows a deep absorption by the parental cloud, but also two less prominent absorptions at 23.4 and 44.5 km s^{-1}, probably due to foreground clouds along the line-of-sight. There is also other spectral lines (HCCCN, $^{34}SO_2$, CH_3CHO and CH_3OH) much weaker than the main CO line.

celerating source is currently increasing the velocity of the filaments, these velocity gradients are likely related with the decay of the velocity of the molecular material or produced by the interaction between the filaments and the environment material (see Section 3.3).

3.3. *Outflow Energetics*

In light of the findings explained in the previous Section 3.2 we assume hereon that the 24 radial filament ensemble constitutes a single outflow entity with a common origin. In this Section we estimate the physical parameters of the ensemble such as mass, momentum and kinetic energy. We follow an analogous procedure to that indicated in Fernández-López et al. (2020) in G5.89-0.39, and consider local thermodynamic equilibrium and optically thin CO emission. To derive the column density of the CO (3-2) transition we use the equation:

$$N_{tot}(CO) = \frac{3h}{8\pi^3\mu_B^2 J} \frac{Q_{rot}\, e^{E_u/kT_{ex}}}{e^{h\nu/kT_{ex}} - 1} \frac{\int T_B dv}{[J_\nu(T_{ex}) - J_\nu(T_{bg})]} =$$

$$= \frac{1.195 \times 10^{14}(T_{ex} + 0.922)e^{33.192/T_{ex}}}{e^{16.596/T_{ex}} - 1} \frac{T_B \Delta v}{J_\nu(T_{ex}) - J_\nu(T_{bg})} \quad (2)$$

In the expression above we use the Planck's constant $h = 6.6261 \times 10^{-27}\, erg\, s$, the dipole moment
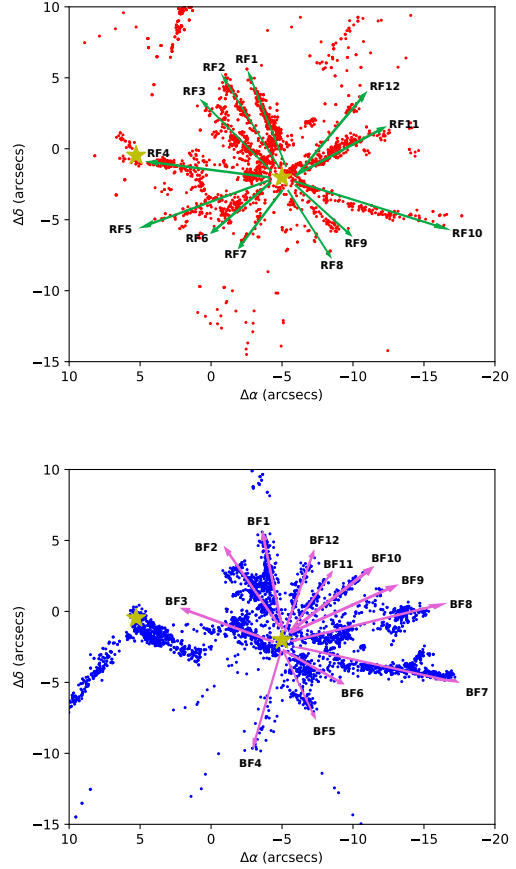

Figure 4. Redshifted (upper panel) and blueshifted (bottom panel) CO(3-2) gas condensations detected in IRAS16076. We could identified 12 redshifted filaments and 12 blueshifted, are labeled as RF and BF respectively. The posible origin of the all filamentes is marked with yellow star.

$\mu_B = 1.1011 \times 10^{-19}\, \text{StatC cm}$, the partition function $Q_{rot} = kT_{ex}/(hB_0) + 1/3$ with a rigid rotor rotation constant $B_0 = 57.635968\, \text{GHz}$, the quantum number of the upper level $J = 3$, the Rayleight-Jeans equivalent temperature $J_\nu(T) = (h\nu/k)/(e^{h\nu/kT} - 1)$, the brightness temperature T_B in K and the velocity interval Δv in km s^{-1}. Regarding the excitation temperature, we take two different values: 40 and 70 K (Felipe Navarete, private communication; see also Navarete et al. (2019)), appropriate for many massive clumps in the Milky Way. We estimate the mass in each velocity channel as:

$$M_{out} = \mu m h \Omega N_{tot}/X_{CO} \quad (3)$$

where μ is the mean molecular weight, which is assumed to be equal 2.76 (Yamaguchi et al. 1999), m is the hydrogen atom mass ($\sim 1.67 \times 10^{-24} g$), Ω is the solid angle, and a CO abundance of $X_{CO}=10^{-4}$. We derive a total mass for the dispersal explosive outflow as the sum of
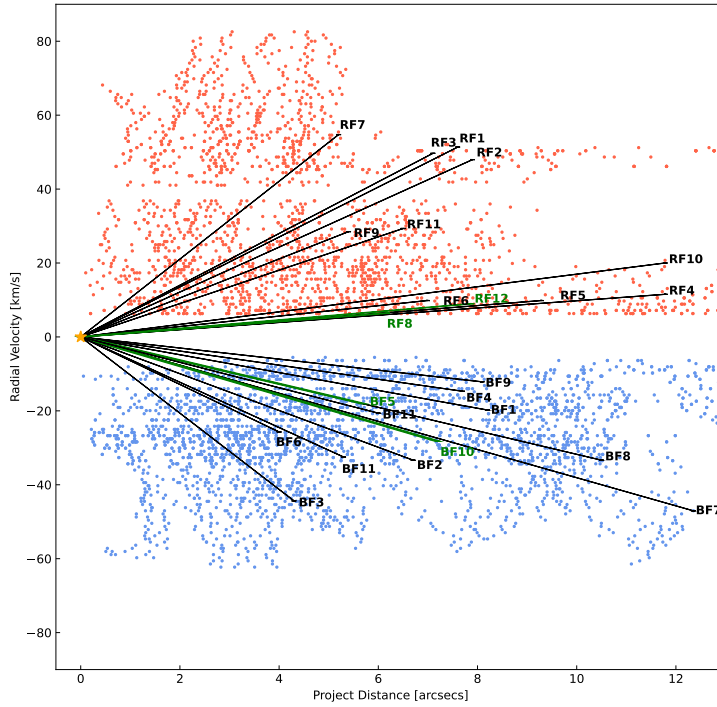
8

Figure 5. Position-Velocity diagram of the CO(2-1) emission from the ensemble of filaments associated with IRAS 16076-5134. The blueshifted and redshifted dots are extracted analyzing the CO condensations of the filamentary outflows emerging from the MM8 dense core. The black straight lines were plot linking the yellow star, placed at the location of MM8 at 0 km s^{-1} (radial velocities given with respect to the cloud velocity) and the tip of every one of the 24 filaments of the ensemble. Better angular resolution is needed for better analysis of filament kinematics.

the masses of the all filaments in each channel (see Table 3). In order not to overestimate the mass measurement, we exclude the channels contaminated by the emission of the parental molecular cloud and the other clouds along the line-of-sight, as well as the channels affected by other molecular lines emission (CH$_3$CHO and unindentified) toward the wing of CO line. Finally, we add all the channel masses to derive a total mass between 138 and 216 $M_\odot$, for 70 K and 140 K respectively.

Recently, Raga et al. (2020) presented an analytical 'head/tail model' that could explain the kinematics found in the explosive Orion BN/KL flow. This model considers an ejected plasmon, where the tail of the plasmon is decelerating due to the interaction with the medium it passes through. The PV diagrams resulting from this model are similar to those of the Orion BN/KL filaments (Zapata et al. 2009; Bally et al. 2017), which show a velocity gradient (the radial velocity increases with projected distance). As a first approximation, we consider a simple scenario, in which the plasmons travel with no friction. Therefore, the plasmons

follow constant velocity trajectories. We also assume that plasmons are ejected isotropically from a common origin. Therefore, the plasmon will follow a roughly constant velocity trajectory, and we also assume that they are ejected isotropically from the origin of the explosion. To better estimate the momentum and kinetic energy it is necessary to take into account the inclination of each filament ($v_{filament} = v_{rad}/cos(i)$, where v_{rad} is the velocity along the line-of-sight and i the inclination with respect to the plane of the sky). But the resolution of the observations does not allow us to obtain information about the inclinations of each filament, so we will take the maximum observed radial velocity (83 km s^{-1}) as the expansion velocity (V$_{outflow}$) of all filaments. With this V$_{outflow}$, we can estimate a lower limit for the dynamic age, momentum and kinetic energy of the outflow. We perform this analysis in Figure 7, which shows a PV diagram similar to Figure 5. On the PV diagram we have superimposed models (green curve and shaded region) of an isotropic expansion at constant velocity varying its dynamic age. Mod-
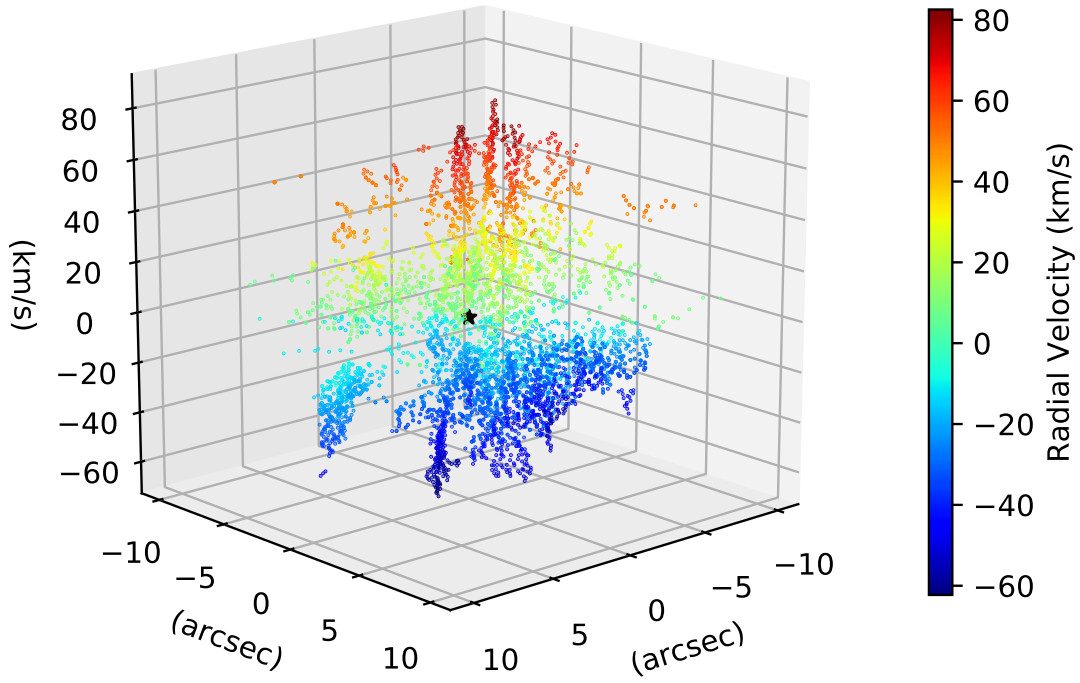
Figure 6. Three-dimensional representation of the dispersal outflowing event in IRAS 16076-5134. The radial blueshifted and redshited velocities are show from blue to red colors. The LSR radial velocity scale-bar (in km s^{-1}) is shown on the right. The (0″, 0″, 0 km s^{-1}) position is the origin of the plot and is marked by a black star, representing the origin of the dispersal outflow.

els of good qualitative agreement are found manually by using $t_{dyn} = 3500 \pm 500$ years. Finally, the derived total outflow momentum are 1.2×10^4 $M_\odot$ km s^{-1} and 1.8×10^4 $M_\odot$ km s^{-1}, and total outflow kinetic energy are 9.9×10^{48} erg and 1.5×10^{49} erg for 70 K and 140 K, respectively. This implies that the outflow emission in I16076 is associated with a very energetic event.

4. DISCUSSION

4.1. *I16076 a New Explosive Dispersal Outflow?*

The outflow found in the high-mass star-forming region I16076 consists of an ensemble of at least 24 radial high-velocity filament-like ejections (ranging from −62 to +83 km s^{-1}) distributed quasi-isotropically. The filaments point back to approximately the same central position, where the MM8 dense core is located (Fig.2). Spatial overlap of the redshifted and blueshifted fila-

ments is observed. The filaments presents a linear velocity gradient (see Fig. 6). In addition, the estimated energy of the filament ensemble is at least one to two order of magnitude larger than that of typical outflows associated with high-mass protostars. All these features point to a direct analogy with those of the explosive dispersal outflows: Orion-KL, DR21 and G5.89-0.39 (e.g., Zapata et al. 2017; Bally 2016; Zapata et al. 2020). The collected evidence strongly suggests that I16076 is a new explosive dispersal outflow candidate. Therefore, the ejection of filaments would have occurred from a single brief energetic event. However, new high-angular and more sensitive observations are needed to confirm it.

4.2. *Rate of Explosive Dispersal Outflows in the Milky Way*

As indicated by the elements explained in Section 4.1 the ensemble of filaments in I16076 could be a new ex-

Table 3. Outflow parameters

Outflow	End Coordinates		V_{end}	Extent	PA
Name	[RA (J2000)]	[Dec (J2000)]	[km s^{-1}]	[arcsec]	[°]
RF1	16 11 26.784	-51 41 50.28	51.36	7.6	18
RF2	16 11 26.976	-51 41 50.28	47.98	7.9	31
RF3	16 11 27.096	-51 41 52.80	49.67	7.1	50
RF4	16 11 27.768	-51 41 56.04	11.55	11.8	85
RF5	16 11 27.456	-51 42 00.00	9.86	9.3	109
RF6	16 11 27.168	-51 42 01.08	9.86	7.0	124
RF7	16 11 26.856	-51 42 01.44	54.75	5.2	146
RF8	16 11 26.208	-51 42 02.52	6.47	6.2	-150
RF9	16 11 26.352	-51 42 00.36	28.49	5.4	-131
RF10	16 11 25.320	-51 42 00.36	20.02	12.2	-106
RF11	16 11 25.968	-51 41 54.24	29.34	6.5	-62
RF12	16 11 25.992	-51 41 51.72	9.01	7.9	-43
BF1	16 11 26.736	-51 41 49.56	-19.78	8.2	13
BF2	16 11 26.880	-51 41 51.72	-33.34	6.7	30
BF3	16 11 26.928	-51 41 55.68	-44.35	4.3	68
BF4	16 11 26.760	-51 42 04.32	-14.70	7.7	164
BF5	16 11 26.304	-51 42 02.16	-18.09	5.7	-156
BF6	16 11 26.256	-51 41 59.64	-25.71	4.0	-133
BF7	16 11 25.272	-51 41 59.64	-46.04	12.5	-102
BF8	16 11 25.488	-51 41 54.96	-33.35	10.5	-77
BF9	16 11 25.800	-51 41 53.52	-12.16	8.1	-62
BF10	16 11 25.968	-51 41 52.80	-28.25	7.2	-51
BF11	16 11 26.232	-51 41 53.16	-32.49	5.3	-36
BF12	16 11 26.376	-51 41 51.72	-20.63	6.0	-16

Figure 7. Models (green curve and shaded region) of good qualitative agreement of an isotropic expansion at constant velocity ($V_{outflow}$=83 km s^{-1}) on the PV diagram setting $t_{dyn} = 3500 \pm 500$ years.

plosive dispersal outflow. The discovery of another of such dispersal events could have further implications, that we explore in this Section. For instance, we do not know accurately how common these dispersal outflows in the Galaxy, if they play a role in the energy budget of the Interstellar Medium, or the physical processes that originate them. Figure 8 shows the spatial distribution of the currently confirmed dispersal outflows in the Milky Way, along with I16076 (red crosses). S106 IR[6], a recently reported possible explosive dispersal outflow (inverted blue triangle, Bally et al. 2022) is also included in the sample. Making a crude estimate, Zapata et al. (2020) derived a frequency rate of one explosive dispersal event every 130 years in the Milky Way, considering Orion BN/KL, DR21 and G5.89-0.39. Assuming that I16076 and S106 IR are explosive dispersal outflows, we can refine this rate estimate. First, assume that the

---

[6] This region has a complex of H_2 and N[III] compact structures with increasing proper motions with projected distance from the young high-mass stellar object, but the nature of these features still needs further confirmation.
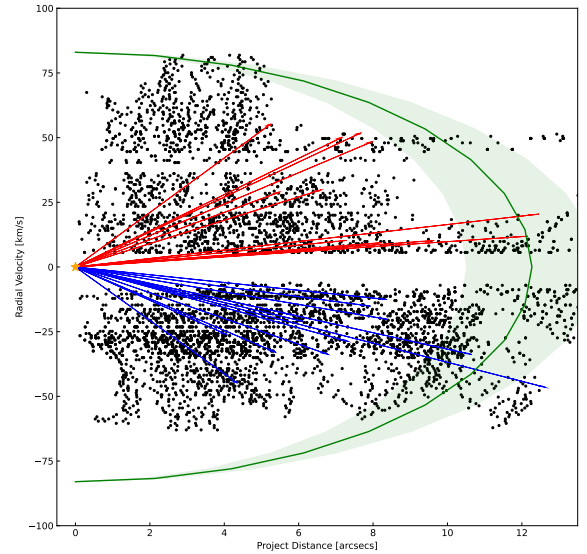
explosive dispersal outflows are evenly spaced in time during the last 15330 years (it is the lapse of time between all 5 outflows, taking into account their different distances to Earth). Second, the dispersal outflows are within a projected circle of 5.6 kpc in diameter (the separation between I16076 and DR21, which are the most separated pair of known dispersal outflows). Finally, extrapolate the frequency rate to the disk of the Galaxy, which we assume as a flat disk with a 15 kpc radius. Since the star formation rate is fairly constant with galactocentric distance (e.g., Urquhart et al. (2014); Nakanishi & Sofue (2006)), and we only have a few explosive outflow cases, the frequency rate obtained will be a crude rate of first order approximation. Under these assumptions, the estimate of the frequency of dispersal outflows in the Galaxy should be regarded as a lower limit. In this manner, we obtain a rate of one dispersal outflow every 110 years. This frequency rate could be even larger with the availability of a more complete high-resolution and high-sensitivity survey (not just targeted observations), which might lead to the identification of more explosive events within the considered radius.

It is worth to note that this frequency rate is comparable to the rate of supernovae (one every 50 years Diehl et al. 2006). This fact may have implications for the energy budget of the Galaxy, even accounting for the ~ 100 times lower amount of energy (10^{49} erg) that
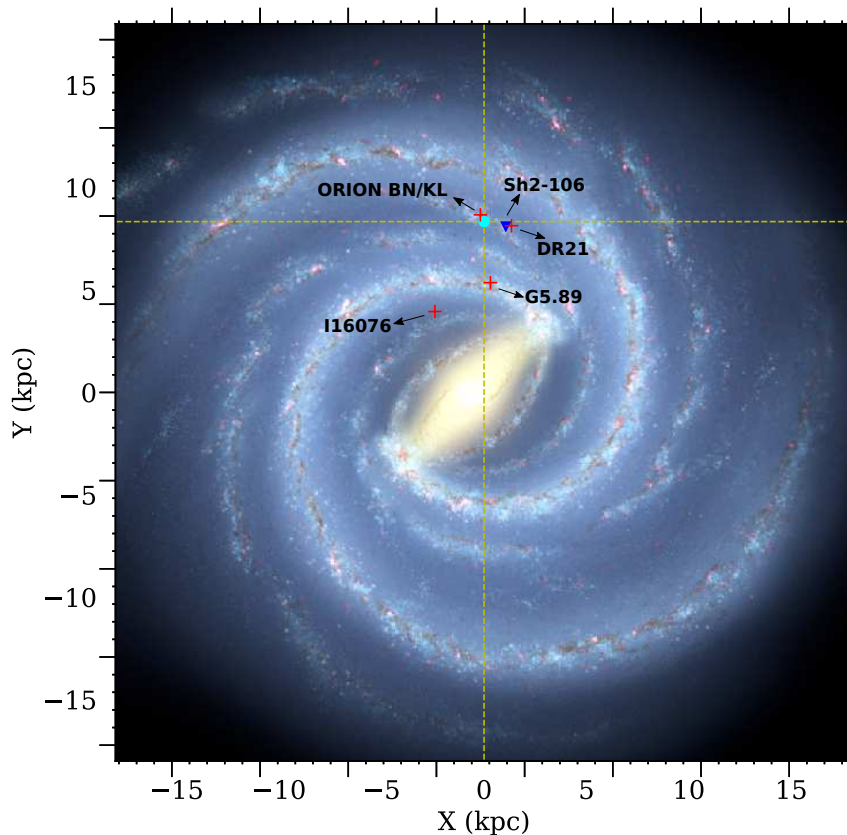
Figure 8. Sketch of the projected spatial distribution of the confirmed explosive dispersal outflows (red crosses), plus S106 IR (blue inverted triangle, Bally et al. 2022) in The Milky Way (artist's concept, R. Hurt: NASA/JPLCaltech/ SSC). The location of the Sun is marked with a circle at the crossing of the two dashed lines.

a dispersal outflow deposits in the Interstellar Medium compared with a core-collapse supernovae that releases energies of 10^{51} erg (Hamuy 2003). The origin of the explosive dispersal outflows is probably associated with the disruption of a massive young non-hierarchical stellar system, and/or with a protostellar collision (Zapata et al. 2009; Bally et al. 2011; Zapata et al. 2013; Rivilla et al. 2014; Bally 2016; Bally et al. 2017). One of its consequences is the ejection of a small group of runaway protostars (e.g., Gómez et al. (2008); Rodríguez et al. (2020)). Hence, there seems to be a link between the origin of the explosive dispersal outflows and the stellar dynamical interactions. The rate of dispersal explosive outflows would show that dynamic interactions and stellar collisions may be a common scenario in high-density clusters that eject runaway stars. Hence, a more complete survey of these kind of outflows may be important to advance our understanding of how massive stars form.

5. CONCLUSIONS

In this paper we presented archival observations of the 0.9 mm continuum and CO (3-2) spectral line emission toward the massive star-forming region IRAS 16076-5134 carried out with ALMA. We found 14 dense cores associated in two small clumps. The cores have masses in the range from 0.3 to 22 $M_\odot$. We found an ensemble of 24 radial filament-like ejections of CO (3-2) line emission (12 blueshifted and 12 redshifted) ranging from -62.15 to $+83.47$ km s^{-1} respect to the cloud velocity (-87.7 km s^{-1}). This filaments are apparently emerging from the neighborhood of the dense core MM8. Also, we reported two more extended North-South monopolar outflows. One blueshifted associated with MM3, and one redshifted launched from an unidentified source.

We analyzed the CO (3-2) morphology and kinematics of the filament ensemble around MM8. The size of the ensemble of filaments is $\sim 20''$ and each filaments are distributed in a radial fashion, quasi-isotropically around a common center located close to the peak emission of MM8. The velocity of filaments shows a velocity

gradient. The velocity increases further away from the common center, as it happens with the fragments of an explosion. Using the integrated CO (3-2) emission we calculate a total mass for the filaments between 138-216 $M_\odot$. Assuming an isotropic expansion model with constant velocity of 83 km s^{-1} and dynamical age of 3500 years, we derive a rough estimate for the momentum and kinetic energy of the gas of the ensemble of filaments. The order of magnitude of the kinematic energy is 10^{48-49} erg. Based on the evidence, we suggest that the ensemble of filaments in IRAS 16076-5134 is an explosive dispersal outflow candidate. Under this hypotheses, we made an raw estimate of the lower limit of the rate of dispersal outflows in the Galaxy considering constant star formation rate and efficiency with respect to the galactocentric radio of the Galaxy. The value obtained is comparable to the rate of supernova explosions, which may have further implications on the role of the energy balance of the dispersal outflows in the Interstellar Medium, and the nature and origin of this kind of outflows in massive star formation.

ACKNOWLEDGEMENTS

REFERENCES

Arce, H. G., Shepherd, D., Gueth, F., et al. 2007, in Protostars and Planets V, ed. B. Reipurth, D. Jewitt, & K. Keil, 245. https://arxiv.org/abs/astro-ph/0603071

Bally, J. 2016, ARA&A, 54, 491, doi: 10.1146/annurev-astro-081915-023341

Bally, J., Chia, Z., Ginsburg, A., et al. 2022, ApJ, 924, 50, doi: 10.3847/1538-4357/ac30de

Bally, J., Cunningham, N. J., Moeckel, N., et al. 2011, ApJ, 727, 113, doi: 10.1088/0004-637X/727/2/113

Bally, J., Ginsburg, A., Arce, H., et al. 2017, ApJ, 837, 60, doi: 10.3847/1538-4357/aa5c8b

Bally, J., Ginsburg, A., Silvia, D., & Youngblood, A. 2015, A&A, 579, A130, doi: 10.1051/0004-6361/201425073

Bally, J., & Zinnecker, H. 2005, AJ, 129, 2281, doi: 10.1086/429098

Baug, T., Wang, K., Liu, T., et al. 2020, ApJ, 890, 44, doi: 10.3847/1538-4357/ab66b6

—. 2021, MNRAS, 507, 4316, doi: 10.1093/mnras/stab1902

Bronfman, L., Nyman, L. A., & May, J. 1996, A&AS, 115, 81

Diehl, R., Halloin, H., Kretschmer, K., et al. 2006, Nature, 439, 45, doi: 10.1038/nature04364

Faúndez, S., Bronfman, L., Garay, G., et al. 2004, A&A, 426, 97, doi: 10.1051/0004-6361:20035755

Fernández-López, M., Zapata, L. A., Rodríguez, L. F., et al. 2020, AJ, 159, 171, doi: 10.3847/1538-3881/ab7a10

Fernández-López, M., Sanhueza, P., Zapata, L. A., et al. 2021, ApJ, 913, 29, doi: 10.3847/1538-4357/abf2b6

Gómez, L., Rodríguez, L. F., Loinard, L., et al. 2008, ApJ, 685, 333, doi: 10.1086/590229

Hamuy, M. 2003, ApJ, 582, 905, doi: 10.1086/344689

Hildebrand, R. H. 1983, QJRAS, 24, 267

Hull, C. L. H., Plambeck, R. L., Kwon, W., et al. 2014, ApJS, 213, 13, doi: 10.1088/0067-0049/213/1/13

Konigl, A., & Pudritz, R. E. 2000, in Protostars and Planets IV, ed. V. Mannings, A. P. Boss, & S. S. Russell, 759. https://arxiv.org/abs/astro-ph/9903168

Liu, T., Kim, K.-T., Yoo, H., et al. 2016, ApJ, 829, 59, doi: 10.3847/0004-637X/829/2/59

Liu, T., Evans, N. J., Kim, K.-T., et al. 2020, MNRAS, 496, 2821, doi: 10.1093/mnras/staa1501

Motte, F., Bontemps, S., & Louvet, F. 2018, ARA&A, 56, 41, doi: 10.1146/annurev-astro-091916-055235

Nakanishi, H., & Sofue, Y. 2006, PASJ, 58, 847, doi: 10.1093/pasj/58.5.847

Navarete, F., Leurini, S., Giannetti, A., et al. 2019, A&A, 622, A135, doi: 10.1051/0004-6361/201629777

Ossenkopf, V., & Henning, T. 1994, A&A, 291, 943

Peng, T. C., Zapata, L. A., Wyrowski, F., Güsten, R., & Menten, K. M. 2012, A&A, 544, L19, doi: 10.1051/0004-6361/201219937

Raga, A. C., Rodríguez-González, A., Hernández-Martínez, L., Cantó, J., & Castellanos-Ramírez, A. 2020, MNRAS, 499, L91, doi: 10.1093/mnrasl/slaa165

Rivera-Ortiz, P. R., Rodríguez-González, A., Cantó, J., & Zapata, L. A. 2021, ApJ, 916, 56, doi: 10.3847/1538-4357/ac05bb

Rivilla, V. M., Jiménez-Serra, I., Martín-Pintado, J., & Sanz-Forcada, J. 2014, MNRAS, 437, 1561, doi: 10.1093/mnras/stt1989

Rodríguez, L. F., Dzib, S. A., Zapata, L., et al. 2020, ApJ, 892, 82, doi: 10.3847/1538-4357/ab7816

Sault, R. J., Teuben, P. J., & Wright, M. C. H. 1995, in Astronomical Society of the Pacific Conference Series, Vol. 77, Astronomical Data Analysis Software and Systems IV, ed. R. A. Shaw, H. E. Payne, & J. J. E. Hayes, 433. https://arxiv.org/abs/astro-ph/0612759

Shu, F. H., Adams, F. C., & Lizano, S. 1987, ARA&A, 25, 23, doi: 10.1146/annurev.aa.25.090187.000323

Shu, F. H., Najita, J. R., Shang, H., & Li, Z. Y. 2000, in Protostars and Planets IV, ed. V. Mannings, A. P. Boss, & S. S. Russell, 789–814

Shu, F. H., Ruden, S. P., Lada, C. J., & Lizano, S. 1991, ApJL, 370, L31, doi: 10.1086/185970

Urquhart, J. S., Figura, C. C., Moore, T. J. T., et al. 2014, MNRAS, 437, 1791, doi: 10.1093/mnras/stt2006

Urquhart, J. S., König, C., Giannetti, A., et al. 2018, MNRAS, 473, 1059, doi: 10.1093/mnras/stx2258

Wenger, T. V., Balser, D. S., Anderson, L. D., & Bania, T. M. 2018, ApJ, 856, 52, doi: 10.3847/1538-4357/aaaec8

Wood, D. O. S., & Churchwell, E. 1989, ApJ, 340, 265, doi: 10.1086/167390

Yamaguchi, R., Akira, M., & Yasuo, F. 1999, in Star Formation 1999, ed. T. Nakamoto, 383–384

Zapata, L. A., Schmid-Burgk, J., Ho, P. T. P., Rodríguez, L. F., & Menten, K. M. 2009, ApJL, 704, L45, doi: 10.1088/0004-637X/704/1/L45

Zapata, L. A., Schmid-Burgk, J., Pérez-Goytia, N., et al. 2013, ApJL, 765, L29, doi: 10.1088/2041-8205/765/2/L29

Zapata, L. A., Schmid-Burgk, J., Rodríguez, L. F., Palau, A., & Loinard, L. 2017, ApJ, 836, 133, doi: 10.3847/1538-4357/aa5b94

Zapata, L. A., Ho, P. T. P., Guzmán Ccolque, E., et al. 2019, MNRAS, 486, L15, doi: 10.1093/mnrasl/slz051

Zapata, L. A., Ho, P. T. P., Fernández-López, M., et al. 2020, ApJL, 902, L47, doi: 10.3847/2041-8213/abbd3f

Zhang, Q., Wang, Y., Pillai, T., & Rathborne, J. 2009, ApJ, 696, 268, doi: 10.1088/0004-637X/696/1/268